Journal of Materials Chemistry B

ROYAL SOCIETY OF CHEMISTRY

PAPER

View Article Online
View Journal | View Issue

Cite this: J. Mater. Chem. B, 2023, 11, 10108

A nanozyme-reinforced injectable photodynamic hydrogel for combating biofilm infection†

Junqing Zhang,[a] Shuang Zhao,[a] Shen Zhang,[a] Hao Zhu,[a] Yaoxin Zhang,[a] Linpei Li,[a] Chaoqun Liu *[ab] and Jiahua Shi *[a]

Received 27th July 2023,
Accepted 4th October 2023

DOI: 10.1039/d3tb01688a

rsc.li/materials-b

Bacterial biofilm-associated infectious diseases remain serious menaces to human health. Recently, photodynamic therapy (PDT) has become a prospective strategy for combating biofilm infection. However, anaerobic conditions in a biofilm greatly inhibit its therapeutic efficacy. Here, a nanozyme-reinforced injectable hydrogel is prepared using Ca^{2+}-crosslinked sodium alginate incorporated with photosensitizer-loaded MnO_2 nanosheets and CaO_2 nanoparticles for O_2 self-sufficient PDT to eradicate biofilm infection. In our design, CaO_2 reacts with water to produce locally concentrated H_2O_2, which could be catalyzed by MnO_2 nanosheets (catalase-mimic nanozymes) to generate O_2 and greatly relieve the hypoxic conditions in the biofilm, thus significantly strengthening PDT efficacy. *In vitro* assays confirmed that the hybrid hydrogel not only exhibits high-performance bactericidal activity in combating both Gram-positive *Staphylococcus aureus* and Gram-negative *Escherichia coli* but also shows great efficacy in eliminating biofilm infection. Moreover, benefiting from its good syringeability, the hybrid hydrogel is prone to fit irregular wounds and exhibits high efficiency in promoting wound healing in a biofilm-infected mice model. Besides, no obvious toxicity is detected in the hybrid hydrogel. Overall, we envision that our designed hydrogel could provide a prospective solution for combating biofilm-associated infections.

Introduction

Bacterial infection is increasingly becoming an international security issue and endangering the health of human beings.[1–5] Antibiotics are still the most widely recognized treatment for bacterial infections in clinics.[6,7] However, the formation of bacterial biofilms intensifies the drug resistance tendency.[8,9] A biofilm is a dense and sticky membranoid substance formed by bacteria and extracellular polymer substance (EPS), including extracellular DNA, proteins, and exopolysaccharides.[10,11] The EPS can not only serve as a shielded parclose to restrain antibiotics' infiltration but also make antibiotics ineffective through specific enzymes.[12,13] Hence, bacteria in biofilms can resist antibiotics 1000 times better than planktonic bacteria.[14,15] Consequently, there is an urgent need to develop promising therapeutic strategies to combat biofilm infection.

Photodynamic therapy (PDT) is a novel therapeutic strategy for treating bacterial biofilm infection.[16,17] This strategy utilizes light-irradiated photosensitizers to produce potent reactive oxygen species (ROS) with the assistance of oxygen (O_2) for oxidizing and killing bacteria,[18,19] offering more advantages such as spatio-temporal controllability, strong specificity and little drug resistance compared to antibiotic therapy.[20] However, PDT efficiency is severely limited due to the anaerobic microenvironment of the bacterial biofilm.[21] Recently, nanozymes have attracted growing interest on account of their excellent stability against harsh environments, low-cost synthesis and adjustable catalytic activities compared to natural enzymes.[22] Notably, catalase-mimic MnO_2 nanozymes have emerged as prominent nanodrugs for supplying O_2 for enhanced PDT, and exhibit good enzymatic activity and benign biocompatibility.[23] Unfortunately, the H_2O_2 concentration in biofilms is too low to supply enough O_2.[24] Although exogenous H_2O_2 could be added to the biofilm to increase the H_2O_2 amount, superfluous H_2O_2 tends to cause injury to healthy tissues.[25,26] Recently, glucose oxidase has been applied to boost the H_2O_2 amount; however, the complex preparation procedure and high-cost limited its further application.[27,28] Hence, there is an urgent need to construct a facile and efficacious O_2 self-sufficient nanozyme-based nanoplatform for improving PDT efficacy in combating biofilm infection.

Here, a nanozyme-reinforced injectable hydrogel is constructed using Ca^{2+}-crosslinked sodium alginate incorporated

[a] School of Pharmacy, Key Laboratory of Natural Medicine and Immune-Engineering of Henan Province, Henan University, Kaifeng, 475004, P. R. China. E-mail: cqliu@henu.edu.cn, sjiahua@henu.edu.cn
[b] Department of Pharmacy, The First Affiliated Hospital of Henan University, Kaifeng, 475001, P. R. China

† Electronic supplementary information (ESI) available. See DOI: https://doi.org/10.1039/d3tb01688a

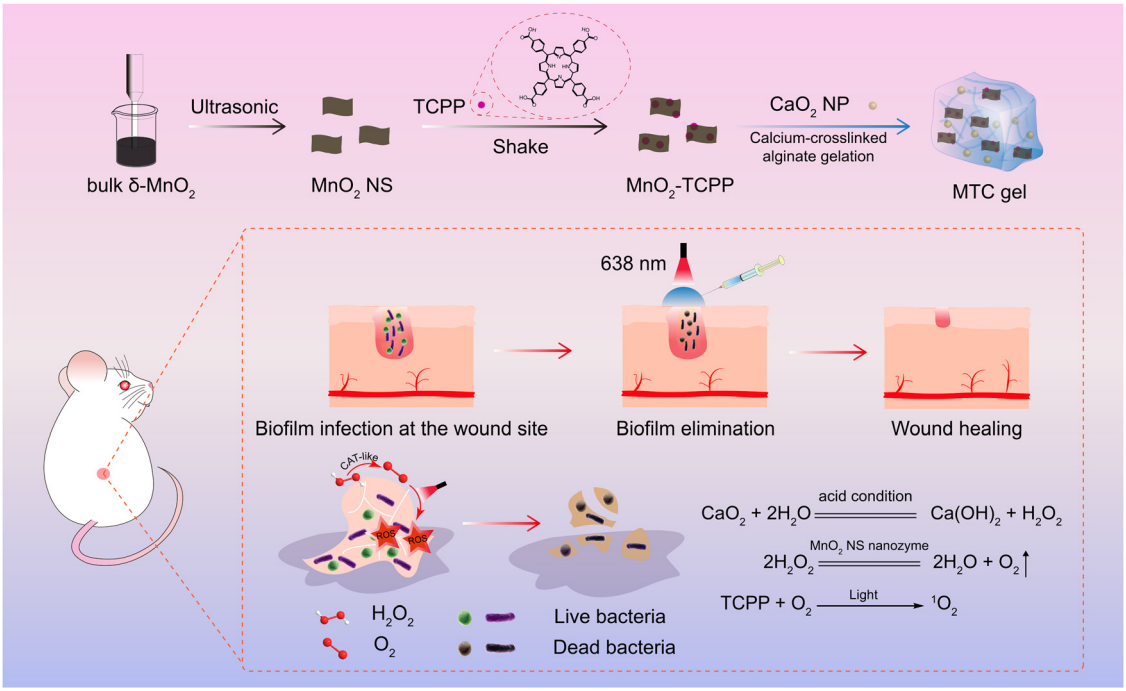

Scheme 1 Schematic illustration of the preparation of a nanozyme-reinforced injectable photodynamic hydrogel which is encapsulated with TCPP-loaded MnO_2 NS and CaO_2 NPs and its detailed mechanism in combating biofilm infection.

with photosensitizer (*meso*-tetra (4-carboxyphenyl) porphine) (TCPP)-loaded MnO_2 nanosheets (MnO_2-TCPP) and CaO_2 nanoparticles (CaO_2 NP) for O_2 self-sufficient PDT to eliminate biofilm infection. Herein, Ca^{2+}-crosslinked sodium alginate is selected as the matrix of the injectable hydrogel for storing MnO_2-TCPP and CaO_2 NP due to its easy preparation, good syringeability and excellent biocompatibility, which can be utilized to filling and adhering on various biofilm-infected sites.[29,30] As illustrated in Scheme 1, CaO_2 NPs are hydrolyzed by water to H_2O_2 under acidic conditions, thus supplying enough H_2O_2 as a substrate of the MnO_2 nanosheet (MnO_2 NS) nanozyme for generating O_2, thereby greatly strengthening PDT efficacy. Of note, the hybrid hydrogel (MTC gel) exhibits high-performance in combating bacteria and biofilm infections both *in vitro* and in a biofilm-infected mice model. Meanwhile, the confined environment of our designed hydrogel makes it easy to remove all the components from the wound after treatment, thereby reducing potential residual toxicity created by the ingredients. Taken together, our designed MTC gel shows huge potential in treating biofilm infection.

Experimental section

Materials

Tetramethyl ammonium pentahydrate ($TMAOH{\cdot}5H_2O$), manganese chloride anhydrous ($MnCl_2$), photosensitizer (*meso*-tetra (4-carboxyphenyl) porphine) (TCPP), PEG-200, H_2O_2 solution, ammonia solution and crystal violet were provided by Sinopharm (Beijing, China). Nutrient agar, trypticase soy broth (TSB) and Dulbecco's modified eagle medium (DMEM) were obtained from Aoboxing Biotechnology (Beijing, China). H_2O_2 test kits, catalase activity test kits, $CaCl_2$ and alginate were acquired from Macklin Biochemical (Shanghai, China). Fluorescent diacetate (FDA), propidium iodide (PI) and 2′, 7′-dichlorofluorescein diacetate (DCFH-DA) were provided by Solarbio (Beijing, China). Enzyme-linked immunosorbent assay (ELISA) kits of interleukin 6 (IL-6) and tumor necrosis factor-α (TNF-α) were purchased from Enzyme-linked Biotechnology (Shanghai, China). *Staphylococcus aureus* (*S. aureus*) (ATCC 25923) and *Escherichia coli* (*E. coli*) (ATCC 25922) strains were obtained from Chuanxiang Biotechnology (Shanghai, China). All the reagents were used without further purification.

Preparation of MnO_2 NS and MnO_2-TCPP

The MnO_2 NS was synthesized by chemical oxidation of Mn^{2+} ions based on a previous method with minor modifications.[31–33] Briefly, $TMAOH{\cdot}5H_2O$ (2.2 g) was dissolved in H_2O_2 (20 mL, 3 wt%). Next, the above solution was quickly transferred into $MnCl_2$ solution (10 mL, 0.3 M) with fast stirring at 1000 rpm. Subsequently, the above solution was reacted at 500 rpm for 0.5 day at 25 °C. Dark brown solution was collected by centrifuging at 2000 rpm for 300 s to obtain a black sediment, which was then rinsed with H_2O 3 times and ethanol 2 times, and then dried by lyophilization for 12 h to obtain bulk δ-MnO_2. To synthesize the MnO_2 NS, bulk δ-MnO_2 was dissolved in deionized water (10 mg mL^{-1}) and sonicated in a probe sonicator (VCX 800, 20 kHz) for 120 min. Finally, the above mixture was centrifuged at 5000 rpm for 600 s to discard the un-exfoliated products at the bottom. The MnO_2 NS in the supernatants was lyophilized and kept in a refrigerator.

For preparing MnO_2-TCPP, MnO_2 NS (10 mg) and TCPP (5 mg) were dissolved in a mixed solution of DMF and water (40 mL, V : V = 1 : 1) and stirred at 25 °C under dark conditions overnight. The dark-purple precipitate (MnO_2-TCPP) was collected *via* centrifugal separation (6000 rpm, 600 s) and rinsed with water and EtOH, separately. After collecting the washing solutions, TCPP loading efficacy was determined *via* UV-Vis spectroscopy.

Synthesis of CaO_2 NP

To prepare CaO_2 NPs,[34] PEG-200 (40 mL) was added to the $CaCl_2$ solution (10 mL, 100 mg mL^{-1}) and stirred for 10 min. Next, H_2O_2 (1.5 mL, 30%) and ammonia solution (1.5 mL, 28%) were added in sequence to the above solution and stirred at 25 °C for 120 min. Finally, CaO_2 NPs were acquired by centrifuging the above mixture and washing with methanol several times. The obtained CaO_2 NP was kept at 4 °C before use.

Synthesis of MTC gel

$CaCl_2$ solution (0.1 M, 0.4 mL) was blended with sodium alginate solution (3 wt%, 5 mL) with gentle manual stirring at room temperature to prepare a colorless Ca-alginate hydrogel (Blank gel).[35] Sodium alginate solution incorporated with MnO_2-TCPP and CaO_2 NPs was blended with $CaCl_2$ solution to acquire a hybrid Ca-alginate hydrogel mixed with MnO_2-TCPP and CaO_2 NPs, named MTC gel. Similarly, MnO_2 gel (Ca-alginate hydrogel only blended with MnO_2 gel), MT gel (Ca-alginate hydrogel only blended with MnO_2-TCPP), CaO_2 gel (Ca-alginate hydrogel only blended with CaO_2 NP) and MC gel (Ca-alginate hydrogel blended with MnO_2 NS and CaO_2 NP) were acquired in the same manner, respectively. The concentrations of MnO_2 NS, MnO_2-TCPP and CaO_2 were 100 μg/ mL^{-1}.

Characterization

Scanning electron microscopy (SEM) images and energy dispersive spectrometry (EDS) spectra were obtained on a Hitachi S-4800 FESEM. Transmission electron microscopy (TEM) images were acquired with a FEI Tecnai G2 F20 with an accelerating voltage of 100 keV. X-Ray diffraction (XRD) analysis was carried out using a Bruker D8 Advance diffractometer with Cu Kα radiation. Atomic force microscopy (AFM) analysis was conducted at Oxford Instruments Asylum Research Inc. The zeta potential was measured using a Malvern Zetasizer Nano ZS90. The UV-Vis spectra were obtained from a Shimadzu UV-2600 UV-Vis spectrophotometer. X-Ray photoelectron spectroscopy (XPS) plots were recorded on a VG Scientific ESCALab 220i-XL electron spectrometer. The O_2 amount was measured using a commercial JPB-607A portable dissolved oxygen meter. Fluorescence images were captured on an Olympus BX-51 fluorescence microscope.

Rheological analysis of MTC gel

The rheological properties of MTC gel were detected by employing a DHR-2 rheometer. Strain sweep and frequency sweep tests were conducted to estimate the storage modulus (G') and loss modulus (G''). More specifically, the strain sweep test was conducted over a strain range from 0.1 to 1000% with a frequency of 10 rad s^{-1}. The frequency sweep experiments were conducted within a frequency range of 1–100 rad s^{-1} under a strain of 1%.

Swelling ratio of MTC gel

MTC gel was immersed in PBS at 37 °C for 10 min and subsequently dried in a vacuum oven at 37 °C for 24 h. Subsequently, swollen MTC gel was taken out and excess water was eliminated using filter paper. The swelling ratio of the hydrogel could be determined based on the following formula:

$$\text{Swelling ratio}\ (\%) = \frac{W_t - W_i}{W_i} \times 100\%$$

where W_t and W_i represent the weight of the swollen MTC gel and the weight of the initial MTC gel, respectively.

H_2O_2 generation from CaO_2 NPs

CaO_2 NPs can be hydrolyzed to H_2O_2 under slightly acidic conditions. To evaluate the H_2O_2 amount, CaO_2 NPs (100 μg mL^{-1}) were placed in PBS (pH 5.3 or 7.4) solution and the H_2O_2 level was detected using a H_2O_2 test kit following the manufacturer's instructions.

Determination of O_2 generation

To evaluate the O_2 generation ability, MnO_2 NS (1 mL, 200 μg mL^{-1}) or MnO_2 gel (1 mL, containing 200 μg mL^{-1} MnO_2 NS) was added to the H_2O_2 solution (1 mL, 1 M) in a centrifuge tube. Oxygen solubility (mg L^{-1}) was continuously monitored using a commercial oxygen meter following the manufacturer's instructions. The O_2 generation ability of the MTC gel (1 mL) was monitored in the same way by replacing the H_2O_2 solution with PBS (1 mL, pH 5.3).

CAT-like activity and kinetics study of MnO_2 NS

H_2O_2 could be decomposed to H_2O and O_2 with the assistance of MnO_2 NS in a dose-dependent manner. The maximum initial velocity (V_{max}) and Michealis–Menten constant (K_m) of MnO_2 NS were then evaluated using a Lineweaver–Burk plot:

$$\frac{1}{V} = \frac{K_m}{V_{max}[S]} + \frac{1}{V_{max}}$$

where V represents the initial velocity and $[S]$ represents the concentration of the substrate, respectively.

Determination of ROS generation

2′,7′-Dichlorofluorescein diacetate (DCFH-DA) was utilized to evaluate the ROS production capacity of MTC gel. Specifically, the NaOH solution (2 mL, 0.01 M) was blended with DCFH-DA (0.5 mL) in DMSO to hydrolyze DCFH-DA to DCFH in the dark for 0.5 h at 25 °C. After that, the PBS (10 mL, pH 7.4) was added to the above solution to obtain a DCFH stock solution. Subsequently, MTC gel was mixed with DCFH (10 μM) and incubated in the dark at 37 °C for 0.5 h. Then, the mixture was irradiated with or without visible light (638 nm, 0.65 W cm^{-2}, 600 s). Subsequently, the solution was

centrifuged, and the supernatant fluorescence intensity was measured using a fluorescence spectrophotometer.

Intracellular ROS detection of MTC gel

Intracellular ROS generation in bacteria was assessed using DCFH-DA as a fluorescent probe. Bacterial solution (1 mL, 10^6 CFU mL^{-1}) was stained with DCFH-DA (10 mM) in the dark at 37 °C for 0.5 h. Then, the bacterial suspension was rinsed three times with PBS. After that, the above suspensions were treated with blank gel, MnO_2 gel, MT gel, CaO_2 gel, MC gel, and MTC gel with or without light illumination (638 nm, 0.65 W cm^{-2}, 600 s), respectively. Finally, bacterial suspensions were spread on glass substrates and imaged using a fluorescence microscope.

Antibacterial assays

The antibacterial efficiency of the MTC gel was evaluated by selecting Gram-positive *S. aureus* and Gram-negative *E. coli* as model bacteria. Bacteria were cultivated in LB medium to restore their proliferative and metabolic capacity. Subsequently, bacteria were harvested by centrifugation, and the bacterial concentration was adjusted with PBS (pH 5.3). Then the above bacterial suspensions (1 mL, 10^6 CFU mL^{-1}) were treated with Blank gel, MnO_2 gel, MT gel, CaO_2 gel, MC gel, and MTC gel with or without laser illumination (638 nm, 0.65 W cm^{-2}, 10 min), respectively. Next, the above suspensions were cultivated at 37 °C before testing the $OD_{600\,nm}$. Finally, bacterial suspensions (100 μL) were evenly spread on the agar plate and cultured at 37 °C for 12 h, and the formed bacterial colonies were counted and photographed.

Live/dead staining analysis was conducted to evaluate the bacterial condition. FDA (live, green) and PI (dead, red) were added to the above bacterial suspensions and kept for 0.5 h. Subsequently, the stained bacteria were obtained by centrifugal separation and rinsed with PBS 3 times.

In vitro biofilm inhibition assay

To culture biofilms, *S. aureus* was incubated in liquid tryptic soy broth (TSB) culture medium (20 mL) and grown overnight at 37 °C by shaking. The diluted *S. aureus* solution (1 mL, 10^6 CFU mL^{-1}) was placed in 24 well plates and cultivated for 1 day at 37 °C by shaking to acquire a biofilm. The medium was removed and replaced with new medium every 24 h, and each well was rinsed with sterile PBS buffer (1 mL, pH 5.3) to eliminate unbound bacteria.

To determine the antibiofilm activity of MTC gel *in vitro*, a bacterial biofilm was treated with various hydrogels with or without laser illumination (638 nm, 0.65 W cm^{-2}, 600 s). Subsequently, the bacteria were separated from various treatments *via* slight sonication for 30 min, diluted 100 times and cultured on agar plates at 37 °C overnight to count colonies.

To measure the biomass of the biofilm, 1 mL of crystal violet dye (0.2%) was added to the biofilm-seeded 24 well plate containing various hydrogels. After 10 min of irradiation, the medium was abandoned and the biofilm was rinsed with PBS. After diluting with 0.5 mL of 95% ethanol, biofilm biomass was quantified at $OD_{590\,nm}$.

A live/dead staining assay was conducted to visually observe the bacterial condition in the biofilm. After treatment with various groups, the remaining biofilm was rinsed 3 times with PBS and stained with FDA (10 μg mL^{-1}) and PI (1 μg mL^{-1}) in the dark for 30 min. Finally, the biofilm rinsed with PBS to eliminate dye and monitored using a fluorescence microscope.

To study the changes of bacterial morphology, after treatment with various groups, the biofilm was fixed by 2.5% glutaraldehyde solution at 4 °C overnight and dehydrated with 30%, 50%, 70%, 80%, 90% and 100% ethanol in turn. Afterwards, SEM was conducted to detect the bacterial morphology.

Hemolysis assay

For evaluating the blood compatibility of the hydrogel, fresh mice blood samples were collected and red blood cells (RBC) were harvested by centrifugal separation (2000 rpm, 600 s). Next, RBCs were dispersed in PBS, and then MTC gel (containing various concentrations of MnO_2-TCPP) was incubated with 2 mL of RBC suspensions at 37 °C for 4 h and then centrifuged at 2000 rpm for 10 min. Finally, the supernatant absorbance was recorded at $OD_{540\,nm}$. The hemolysis ratio of blood cells was obtained according to the formula below:

$$\text{Hemolysis ratio}\,(\%) = \frac{A_M - A_C}{A_P - A_C} \times 100\%$$

where A_M (MTC gel group), A_C (control group) and A_P (positive group) are the absorbance values of RBC samples treated with MTC gel, PBS and deionized water, respectively.

Cytotoxicity assay

For estimating the cytotoxicity of MTC gel, gel leachate was obtained first by incubating MTC gel (containing various concentrations of MnO_2-TCPP) with DMEM (1 mL) at 37 °C overnight. Next, L929 cells were seeded on a 96 well cell plate with 1×10^4 cells per well overnight, followed by replacing it with the above medium. After incubating for 24 h, the medium was discarded and the cells were rinsed several times with PBS. Subsequently, MTT solution (10%) in DMEM was added to each well and incubated for 4 h. Then, the supernatant was abandoned and DMSO (100 μL) was added. Finally, a microplate reader was utilized to detect the absorbance value with a detection wavelength of 570 nm and a reference wavelength of 630 nm.

In vivo anti-biofilm infection experiments

Kunming mice (about 20 g) were purchased from the Medical Animal Center of Zhengzhou University (Zhengzhou, China). All animal experiments approved by the Animal Care and Use Committee of Henan University (Kaifeng, China). To assess whether 638 nm was enough to penetrate the skin tissue biofilm for generating ROS, pork tissue (1 mm) was placed above the MTC gel solution (containing ROS probe DCFH), and subsequently, the pork tissue was irradiated with or without visible light (638 nm, 0.65 W cm^{-2}, 600 s). The supernatant fluorescence intensity was measured using a fluorescence spectrophotometer. As for the treatment process, mice were

first randomly divided into 14 groups (n = 5): (I) PBS, (II) Blank gel, (III) MnO_2 gel, (IV) MT gel, (V) CaO_2 gel, (VI) MC gel, (VII) MTC gel, (VIII) PBS + Light, (IX) Blank gel + Light, (X) MnO_2 gel + Light, (XI) MT gel + Light, (XII) CaO_2 gel + Light, (XIII) MC gel + Light and (XIV) MTC gel + Light. Next, full-thickness skin wounds with a diameter of 6 mm were created on mice back and inoculated with *S. aureus* suspension (100 μL, 10^6 CFU mL^{-1}) for 1 day to establish the *S. aureus*-biofilm-infected wound model. After that, all above wounds were treated with various groups and covered with gauzes for 1 day. The wound sites for light-irradiated groups were subjected to irradiation (638 nm, 0.65 W cm^{-2}, 10 min). During the treatments, wound areas were photographed on day 0, 3, 6, 9 and 12 to evaluate wound healing efficiency. Mice weights were also measured daily. Lastly, to assess the antibiofilm efficacy of MTC gel, all mice were sacrificed on day 12 and the wound tissues were separated, immersed in PBS and bacterial growth was evaluated using a plate coating method. Moreover, wound tissues were stained with crystal violet, rinsed with ethanol and placed into a 24 well plate. To observe the inflammation and epidermal regeneration in the wound area, wound tissues were subjected to hematoxylin and eosin (H & E) and Masson staining for histology analysis, and immunohistochemical staining of IL-6 and TNF-α. Finally, the levels of inflammatory factors (IL-6 and TNF-α) were quantified through commercial ELISA kits.

To evaluate the biosafety of hydrogels, major organs of mice were harvested and the collected tissues were fixed with 4% paraformaldehyde and embedded in paraffin, sectioned, and stained with H&E for further histology analysis. Moreover, blood samples of various groups were collected to conduct a blood routine test and blood biochemical analysis.

Statistical analysis

All data in this article were reported as mean result ± standard deviation. Statistical evaluation was conducted *via* analysis of variance (Student's t-test) using Origin 8.0 software. A p-value < 0.05 was considered statistically significant.

Results and discussion

Fabrication and characterization of MnO_2 NS, MnO_2-TCPP and CaO_2 NPs

A two-dimensional MnO_2 NS was prepared according to the previous report.[32] As revealed by TEM, DLS and AFM, MnO_2 NS exhibited a typical sheet structure with a hydrodynamic diameter of about 300 nm, while the thickness was around 3–4 nm (Fig. 1a–c and Fig. S1, S2, ESI†). Moreover, X-ray diffractometry (XRD) spectra and high-resolution TEM (HRTEM) images were further used to gain insight into the phase structures of the MnO_2 NS powder sample (Fig. S3a, ESI†). The typical peaks of birnessite type of bulk δ-MnO_2 and MnO_2 NS were detected (Fig. 1d and Fig. S4, ESI†), and the lattice spacing of 0.24 nm in the HRTEM image (Fig. S5, ESI†) could be attributed to the (311) facet of the cubic phase MnO_2 NS (JCPDS card no. 42-1169), which was in accordance with the related XRD pattern. Moreover, the MnO_2 NS showed an absorption peak at 380 nm

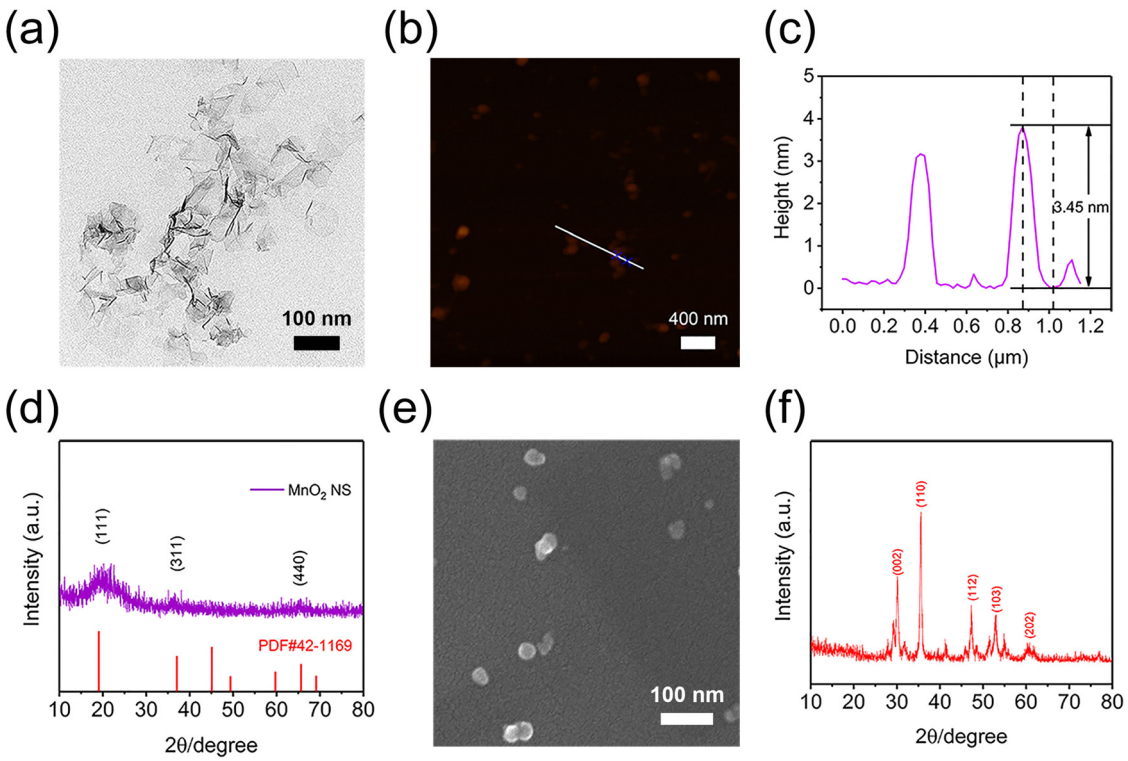

Fig. 1 Characterization of MnO_2 NS and CaO_2 NPs. (a) TEM image of MnO_2 NS. (b) AFM image and (c) the corresponding height image of MnO_2 NS dispersed on a mica substrate. (d) XRD patterns of bulk δ-MnO_2 and MnO_2 NS. (e) SEM image and (f) XRD pattern of CaO_2 NPs.

(Fig. S6, ESI†), this could be assigned to the d–d transition of Mn ions in MnO_6 octahedra of the MnO_2 NS.[32,36] The above results confirmed the successful preparation of MnO_2 NS. To load TCPP, MnO_2 NS and TCPP were dispersed in a DMF/H_2O mixed solution, stirred at 25 °C under dark conditions overnight and lyophilized to obtain MnO_2-TCPP powder (Fig. S3b, ESI†). The TCPP loading efficacy was calculated to be 8.5% based on the standard curve of TCPP (Fig. S7, ESI†). The successful loading of TCPP was further confirmed by EDS and XPS. As shown in Fig. S8 and S9 (ESI†), a distinct enhancement of the N element was observed both in EDS and XPS spectra, which could be attributed to the inherent N element obtained from TCPP. Herein, it should be noted that a small amount of N element in MnO_2 NS originated from tetramethylammonium hydroxide pentahydrate during the synthesis process. These results collectively proved that TCPP can effectively bind to MnO_2 NS. Moreover, no obvious change in morphology was detected before and after TCPP binding (Fig. S10, ESI†), indicating that the loading of TCPP did not affect the sheet structure of MnO_2 NS. As for CaO_2 NPs (Fig. S3c, ESI†), the synthesized CaO_2 NPs exhibited a consistent size distribution around 30 nm with a patchily spherical morphology (Fig. 1e). The XRD pattern of CaO_2 indicated representative diffraction peaks at 30.3°, 35.5°, 47.2°, 47.2° and 60.3° (Fig. 1f), which was consistent with the reported literature studies,[37] confirming that CaO_2 NPs were successfully prepared.

Preparation and characterization of injectable MTC gel

Injectable MTC gel was constructed using a Ca^{2+} crosslinked alginate solution incorporated with MnO_2-TCPP and CaO_2 NP (Fig. 2a). Here, a vial tilt test was utilized to evaluate the formation of MTC gel and the results showed that MTC gel exhibited a homogenous solid form (Fig. 2b and Fig. S11, ESI†). Subsequently, to evaluate the rheological performance and mechanical strength property of MTC gel, G' and G'' were assessed using the strain sweep test and frequency scanning test. As shown in Fig. 2c, at the beginning of measurement, G' was larger than G'', and with an increase in strain, G' and G'' converged at various points, signifying a transition from gel state to sol state, indicating that MTC gel was formed and its

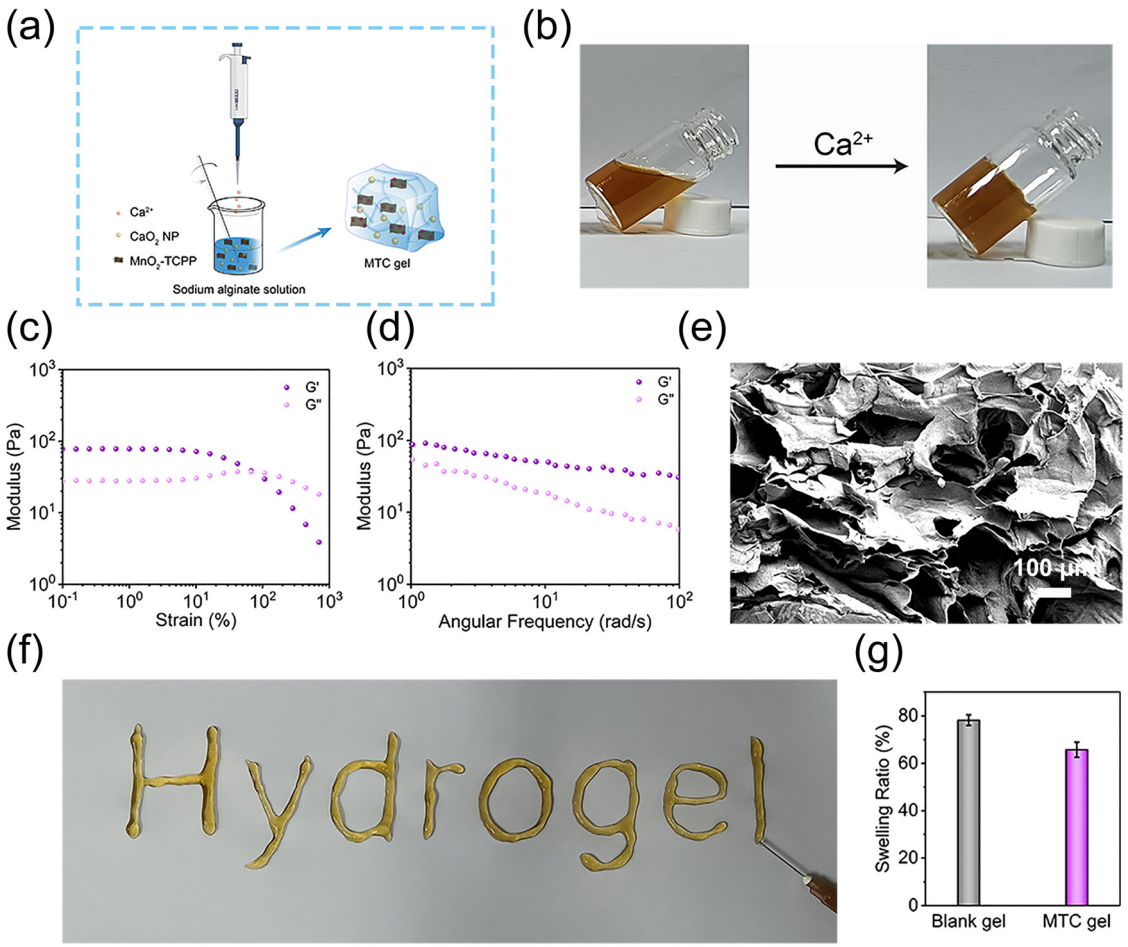

Fig. 2 (a) Schematic illustration for the preparation process of the injectable MTC gel *via* a Ca^{2+}-crosslinked alginate solution incorporated with MnO_2-TCPP and CaO_2 NPs. (b) Digital photographs of the sol–gel phase transformation process of MTC gel. (c) G' and G'' of MTC gel in a dynamic strain sweep. (d) Frequency-dependent shear rheology of MTC gel. (e) SEM image of MTC gel. (f) Digital image of characters "Hydrogel" on blank paper made using a needle containing MTC gel. (g) Swelling ratios of Blank gel and MTC gel (n = 3).

structure was intact and could bear relatively large deformations. Meanwhile, a liquid-like state hydrogel exhibited once the strain beyond 67.5% ($G'' > G'$), indicating that MTC gel was suitable for injection. To further evaluate the rheological properties of MTC gel, G' and G'' were measured across a range of strain values (Fig. 2d), and the broad linear viscosity region confirmed the stability of the three-dimensional network in MTC gel. MTC gel with good mechanical properties could adapt to the stretch of irregular wound tissues. The characters "Hydrogel" could be smoothly written using a syringe equipped with a 21-gauge needle, which could visually prove the good injectable nature of MTC gel (Fig. 2f). Moreover, SEM images of the hybrid hydrogel presented in Fig. 2e clearly displayed its three-dimensional porous morphology. As the swelling feature of hydrogel is essential for the superficial wound healing process, the swelling ratio of MTC gel was evaluated after immersing it into PBS for 1 day, and the result was determined to be 65.75% (Fig. 2g), confirming that it owned some level of moisture absorption capacity.

Generation of H_2O_2, O_2 and ROS of MTC gel

In MTC gel, CaO_2 NPs could be hydrolyzed into H_2O_2 under slightly acidic conditions, and H_2O_2 could be served as the substrate of MnO_2 nanozymes to produce O_2 for enhancing the PDT efficiency, which is vividly described in Fig. 3a. Next, colorimetry was conducted to measure the H_2O_2 production behavior. As shown in Fig. 3b, c and Fig. S12 (ESI†), much more H_2O_2 was produced in PBS at pH 5.3 (simulating pH of biofilm-infected tissue) than that in PBS at pH 7.4 (simulating pH of healthy tissue), indicating that CaO_2 NPs could induce H_2O_2 generation efficaciously at weak acid biofilm-infected tissue. Subsequently, a dissolved oxygen analyzer was utilized to evaluate the amount of O_2 generation from MTC gel. As shown in Fig. 3d and Fig. S13 (ESI†), O_2 could be effectively produced from MnO_2 NS + H_2O_2, MnO_2 gel + H_2O_2 and MTC gel, suggesting that the MnO_2 NS kept its nanozyme activity in MTC gel. The detailed mechanism of MnO_2 NS as a catalase-mimic is shown in Fig. S14 (ESI†), which was realized by the transformation of valence states in manganese.[38,39] Next, an ammonium molybdate method was conducted to further evaluate the catalase mimic activity of MnO_2 NS, as shown in Fig. S15 (ESI†), and the Michealis–Menten constant (K_m) and maximum initial velocity (V_{max}) were calculated by utilizing the Lineweaver–Burk plot, resulting in values of 70.76 μmol L^{-1} and 0.03384 μmol s^{-1}, respectively. Finally, DCFH-DA was utilized to assess the ROS production ability of MTC gel. As shown in Fig. 3e, the light-irradiated MTC gel possessed better ROS generation property than light-irradiated MT gel, suggesting that O_2 self-sufficient MTC gel may be useful for improving the PDT efficacy in treating hypoxic biofilm infection.

Antibacterial activity *in vitro*

Having confirmed the good ROS production ability, the antibacterial properties of MTC gel against *S. aureus* and *E. coli* were evaluated through the growth inhibition assay, spread plate method, live/dead staining assay and intracellular ROS

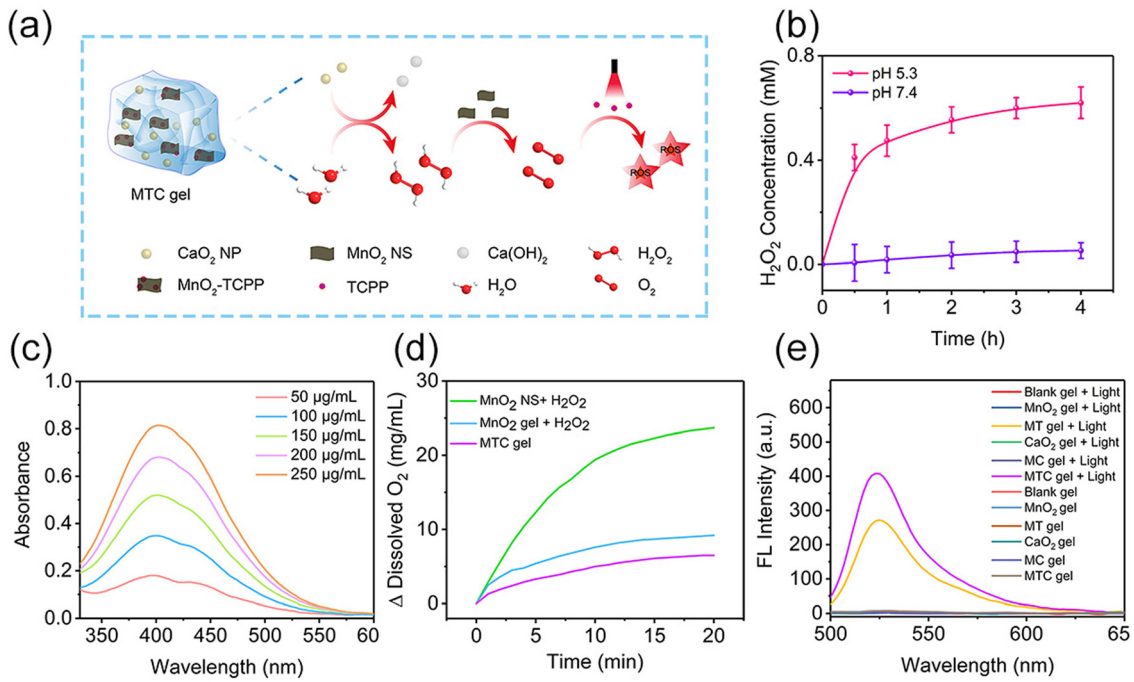

Fig. 3 Release properties of H_2O_2, O_2 and ROS. (a) Schematic illustration of H_2O_2, O_2 and ROS production process. (b) Release profiles of H_2O_2 from CaO_2 NPs (100 μg mL^{-1}) under different pH conditions (n = 3). (c) H_2O_2 produced from various concentrations of CaO_2 NPs at pH 5.3 for 6 h. (d) O_2 produced from pure MnO_2 NS + H_2O_2, MnO_2 gel + H_2O_2 and MTC gel. (e) Release profiles of ROS from various groups of hydrogels with or without light irradiation (0.65 W cm^{-2}, 10 min).

level analysis, and the antibacterial process is illustrated in Fig. 4a. The experimental groups were divided into 14 groups, including PBS, Blank gel, MnO_2 gel (hydrogel doped only with MnO_2 NS), MT gel (hydrogel doped with MnO_2-TCPP), CaO_2 gel (hydrogel doped only with CaO_2 NP), MC gel (hydrogel doped with MnO_2 NS and CaO_2 NP) and MTC gel (hydrogel doped with MnO_2-TCPP and CaO_2 NP). Groups treated with light irradiation were expressed as PBS + Light, Blank gel + Light, MnO_2 gel + Light, MT gel + Light, CaO_2 gel + Light, MC gel + Light and MTC gel + Light, respectively. We first evaluated the antimicrobial ability of MTC gel on *S. aureus*, as shown in Fig. 4b, and no distinct bacterial-killing phenomenon was detected for PBS, PBS + Light, Blank gel, Blank gel + Light, MnO_2 gel, MnO_2 gel + Light, MT gel, MT gel + Light, CaO_2 gel, CaO_2 gel + Light, MC gel, MC gel + Light and MTC gel groups, indicating that all hydrogel groups possessed negligible activity. Moreover, for the MT gel + Light group, bacterial viability decreased to 52.3%, which was attributed to the photodynamic effect of TCPP. Remarkably, a strong bacterial inhibition behavior (99.2%) was detected for the MTC gel + Light group, confirming that the self-generation of O_2 could greatly enhance the photodynamic effect of MTC gel by utilizing the catalase mimic property of MnO_2 NS and H_2O_2 generation ability of CaO_2. Furthermore, the spread plate method displayed similar results (Fig. 4c), suggesting that the light irradiation of MTC gel led to the lowest bacterial count. Additionally, a live/dead staining assay was conducted to further investigate the status of *S. aureus*. Green fluorescence represented live bacteria, while the red fluorescence indicated dead bacteria. As illustrated in Fig. 4d, in the MTC gel + Light group, nearly all bacteria showed red fluorescence, on the contrary, other groups displayed obvious green fluorescence, demonstrating that light illuminated MTC gel possessed best antimicrobial activity. Finally, DCFH-DA was utilized to evaluate the intracellular ROS level in *S. aureus*. As depicted in Fig. 4e, evident green fluorescence was detected for the MT gel + Light and MTC gel + Light group, and the MTC gel + Light group possessed stronger fluorescence, which was consistent with cell-free ROS detection results shown in Fig. 4e, confirming that the MTC gel + Light group showed excellent photodynamic effects. Similar bactericidal results could also be detected for *E. coli* (Fig. S16–S19, ESI†). Consequently, our designed O_2 self-sufficient photodynamic MTC gel demonstrated superior broad-spectrum bactericidal ability upon light illumination.

Anti-biofilm activity *in vitro*

As light-irradiated MTC gel showed remarkable antibacterial efficiency in eliminating planktonic bacteria, we next evaluated the feasibility of MTC gel for combating biofilm infection *in vitro*. Herein, *S. aureus* and *E. coli* biofilms were chosen as two models to investigate the *in vitro* anti-biofilm behavior of MTC gel. The detailed antibiofilm process is shown in Fig. 5a. For *S. aureus*, first, a plate count assay was performed to assess the bacterial viability in the biofilm. As shown in Fig. 5b, no distinct changes in the colony-forming units (CFUs) were detected after coincubation with PBS, Blank gel, MnO_2 gel, CaO_2 gel and MC gel without or with light, respectively, indicating that these groups showed inappreciable antibiofilm activity. However, least CFUs were detected after coincubation with the MTC gel + Light group, and this could be attributed to the generation of a large amount of toxic ROS through an O_2 self-sufficient PDT process. Furthermore, a live/dead bacterial cell staining assay was conducted to further assess the bacterial status in the biofilm (Fig. S20, ESI†). The results demonstrated that the MTC gel + Light group exhibited the most notable red fluorescent signal, which was consistent with the spread plate method results. To appraise the antibiofilm activity of MTC gel, biofilm biomass was quantified using a crystal violet stained colorimetric method. As depicted in Fig. 5c, *S. aureus* biofilm biomass was enormously reduced after coincubation with the MTC gel + Light group; also, Fig. 5d shows the photographs of the crystal violet stained biofilm and the results indicated that the biofilm color for the MTC gel + Light group was much lighter than the other groups, further confirming that light illuminated MTC gel could greatly improve *in vitro* antibiofilm potency. Finally, SEM characterization was employed to explore the bactericidal mechanism of MTC gel on *S. aureus* in the biofilm. As illustrated in Fig. 5e, no change in distinct bacterial morphology was observed for PBS, PBS + Light, Blank gel, Blank gel + Light, MnO_2 gel, MnO_2 gel + Light, MT gel, MT gel + Light, CaO_2 gel, CaO_2 gel + Light, MC gel, MC gel + Light and MTC gel groups, confirming that all hydrogel groups exhibited negligible toxicity toward *S. aureus* in the biofilm. Conversely, the morphology of *S. aureus* in the biofilm changed to a slightly rough and wrinkled morphology. However, treated with the MTC gel + Light group, the cells were seriously wrinkled and even collapsed, which might be attributed to the enhanced generated ROS that dramatically oxidize the *S. aureus* membrane. Similar biofilm elimination ability of MTC gel could be found for the *E. coli*-formed biofilm (Fig. S21–24, ESI†). These results demonstrated that MTC gel exhibited significant *in vitro* anti-biofilm ability toward both Gram-positive and Gram-negative bacteria-formed biofilms.

In vivo treatment of biofilm infections

The distinguished anti-biofilm performance of MTC gel *in vitro* encouraged us to investigate its application as a biofilm eliminator *in vitro*. In this design, we first established a 6 mm diameter full-thickness *S. aureus* biofilm-infected mice wound model. The whole treatment process is depicted in Fig. 6a. Mice were randomly divided into 14 groups, containing PBS, Blank gel, MnO_2 gel, MT gel, CaO_2 gel, MC gel, MTC gel, PBS + Light, Blank gel + Light, MnO_2 gel + Light, MT gel + Light, CaO_2 gel + Light, MC gel + Light and MTC gel + Light. All hydrogels were wiped away 1 day after various treatments. We first assessed whether 638 nm was enough for skin wound biofilm penetration by applying pork tissue (1 mm) as a model. As shown in Fig. S25 (ESI†), the MTC gel + Light group showed much higher ROS fluorescence intensity than the other groups, indicating 638 nm was enough for biofilm penetration in our study. Next, mice wound conditions were evaluated. As illustrated in Fig. 6b, in control groups, mice wounds exhibited distinct skin

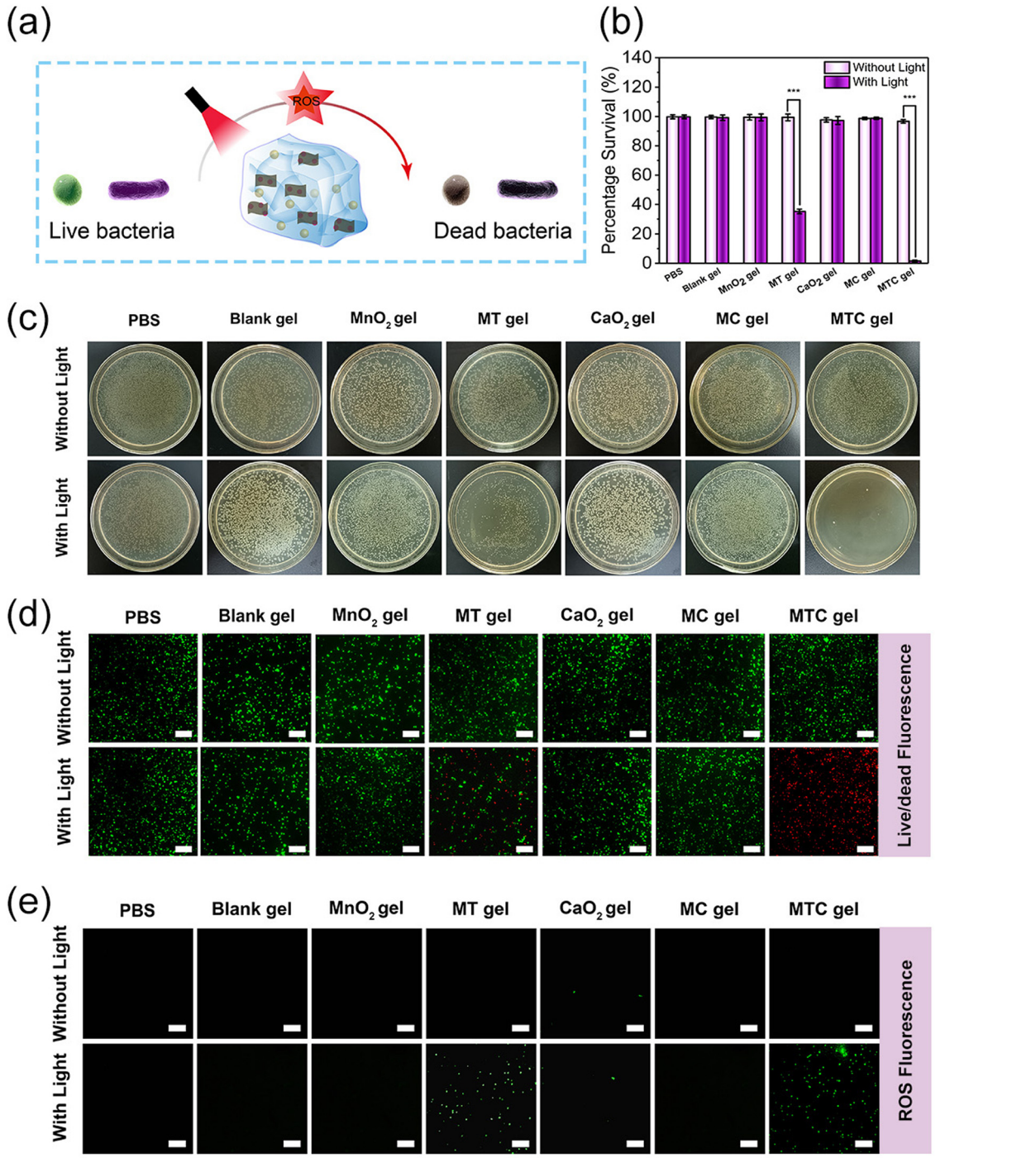

Fig. 4 Antimicrobial abilities of MTC gel *in vitro*. (a) Schematic illustration for the mechanism of MTC gel in combating planktonic bacteria. (b) Percentage survival of *S. aureus* after coincubation with Blank gel, MnO_2 gel, MT gel, CaO_2 gel, MC gel, MTC gel with or without light (0.65 W cm^{-2}, 10 min, $n = 3$, $^{*}P < 0.05$, $^{**}P < 0.01$, $^{***}P < 0.001$). (c) Photographs of the corresponding colonies exhibited the impact of various groups on the growth of *S. aureus*. (d) Live/dead fluorescence images of *S. aureus* stained by FDA (green, live bacteria) and PI (red, dead bacteria) after various therapies. Scale bar: 20 μm. (e) Intracellular ROS fluorescence images (green) of *S. aureus* labelled *via* DCFH-DA after various therapies. Scale bar: 20 μm.

inflammation and epidermal thickening, while the MTC gel + Light groups exhibited a minimum wound area with no significant ulcerative inflammation. Moreover, the treatment effect of MTC gel was also assessed by measuring the real-time variety of wound areas. As illustrated in Fig. 6c and Fig. S26 (ESI†), the MTC gel + Light group possessed the smallest wound area of 5.45%, confirming that the MTC gel + Light group exhibited superior wound closure effect. To appraise the antibiofilm ability of MTC gel, after 12 days treatment, mice wound tissues of various groups were harvested and a spread plate assay was

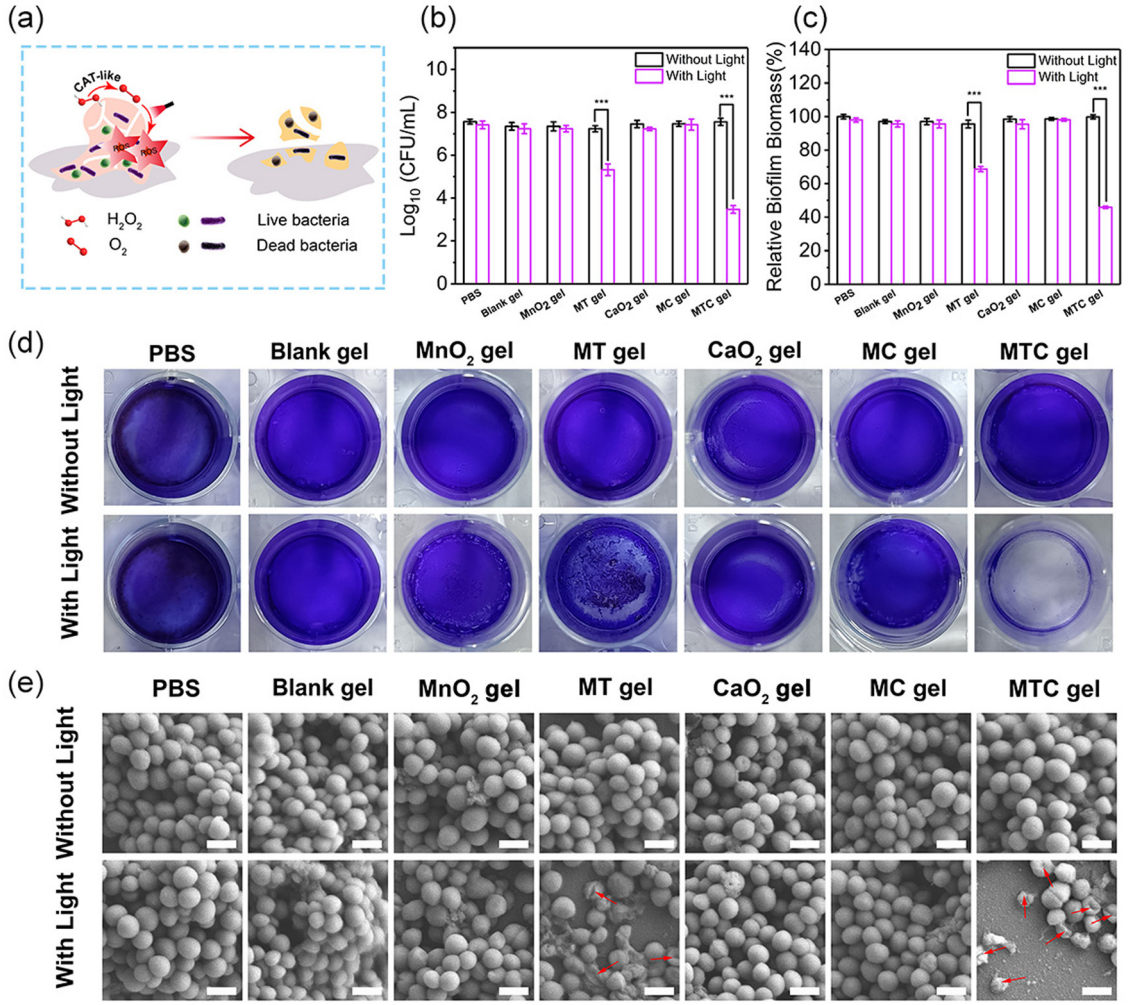

Fig. 5 Anti-biofilm activities of MTC gel *in vitro*. (a) Schematic illustration of the anti-biofilm mechanism of MTC gel. (b) Number of live *S. aureus* in the biofilm after various treatments. (c) Relative biofilm biomass of *S. aureus* biofilms after different therapies (n = 3, $^*P < 0.05$, $^{**}P < 0.01$, $^{***}P < 0.001$). (d) Photographs of the *S. aureus* biofilm stained by crystal violet after different therapies. (e) SEM images of the *S. aureus* biofilm after various therapies. The red arrows show morphological damage of bacteria in the biofilm. Scale bar: 1 μm.

conducted to assess the bacterial amount. As shown in Fig. 6c and Fig. S27 (ESI†), the MTC gel + Light group possessed least number of bacteria, while still plenty of bacteria could be detected for the other groups. Moreover, the antibiofilm ability of MTC gel *in vivo* was further evaluated by staining the wound tissue biofilm with crystal violet, rinsing with ethanol and placing it into a 24 well plate. As shown in Fig. S28 (ESI†), dark violet solutions could be found for control groups, while the color was very light for the MTC gel + Light group. These results were in accordance with *in vitro* biofilm biomass assays (Fig. 5c), showing that the MTC gel + Light group possessed best antibiofilm activity. At the same time, skin tissues were also stained by H&E to further investigate the skin regeneration ability of MTC gel. As depicted in Fig. 6e, following a 12-day treatment, H&E staining results indicated that the MTC gel + Light group-treated mice showed typical morphological features with healthy hair follicles and few inflammatory cells and granulation tissue edemas, demonstrating its good tissue reconstruction ability. Nevertheless, the other groups still presented distinct skin morphological characteristics of inflammatory cells' infiltration and epithelial structure thickening, indicating poor wound healing ability. To gain more insight into the wound healing process of mice after treatments, inflammatory factors' levels (IL-6 and TNF-α) in wound tissues were further evaluated by immumohistochemical staining and by using the ELISA kit. As illustrated in Fig. 6e and Fig. S29 (ESI†), much fewer inflammatory cells were observed and the release of proinflammatory mediators had shifted down obviously in light irradiated MTC gel, suggesting that the MTC gel + Light group could effectively control wound inflammation. Finally, Masson staining was conducted to assess collagen deposition in regenerated skin wound tissues (Fig. 6e). The highest collagen fiber content was disclosed in the MTC gel + Light treated wound skin, illustrating that the MTC gel + Light group possessed densely structured and organized collagen fibers. Conversely, collagen fibers in other groups appeared

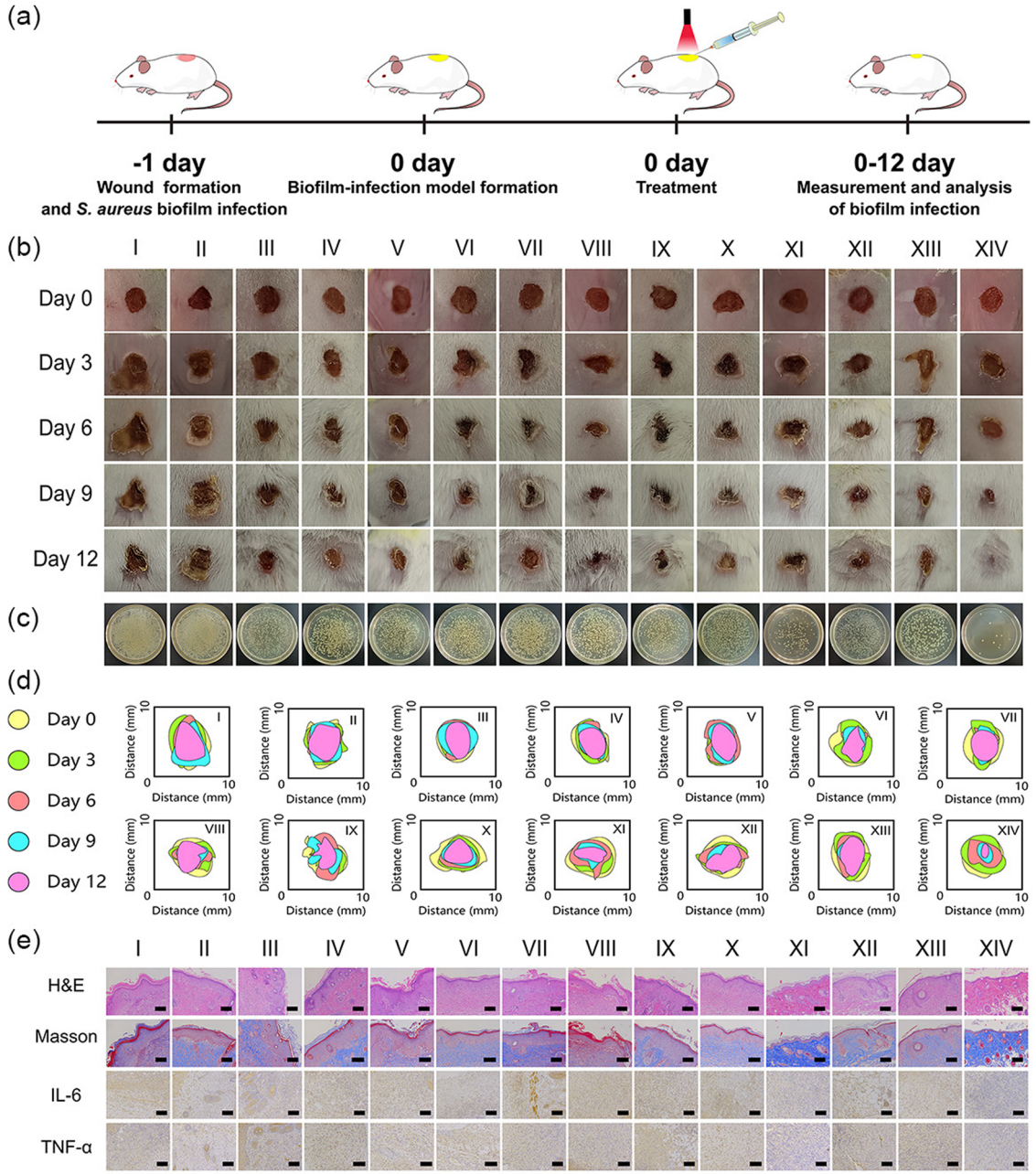

Fig. 6 *In vivo* therapeutic efficacy of MTC gel. (a) Schematic illustration of the establishment and subsequent treatments of the *S. aureus* biofilm-infected wound model in mice. (b) Photographs of *S. aureus* biofilm-infected tissues. (c) Photographs of *S. aureus* colonies obtained from wounds after various therapies. (d) Schematic diagram depicting the change in wound size from day 0 to day 10 after various therapies. (e) H&E and Masson staining slices of wound tissues after various treatments at day 12. Scale bar is 100 μm. (I) PBS, (II) Blank gel, (III) MnO_2 gel, (IV) MT gel, (V) CaO_2 gel, (VI) MC gel, (VII) MTC gel, (VIII) PBS + Light, (IX) Blank gel + Light, (X) MnO_2 gel + Light, (XI) MT gel + Light, (XII) CaO_2 gel + Light, (XIII) MC gel + Light and (XIV) MTC gel + Light. Scale bar: 100 μm.

disorganized and had lower density. Based on the comprehensive analysis above, MTC gel as a moist dressing can provide a wet and healthy environment to effectively eliminate biofilm infection and accelerate wound healing *in vivo*.

Biosafety evaluation

To assess the *in vitro* and *in vivo* biocompatibility of MTC gel, we conducted several experiments including hemolysis assay, cytotoxicity assay, weight monitoring, blood analysis and histological analysis. As depicted in Fig. S30 and S31 (ESI†), no significant hemolysis or cell toxicity was detected, indicating that MTC gel exhibited excellent cytocompatibility. For *in vivo* biocompatibility experiments, no notable change in body weight was observed (Fig. S32, ESI†), confirming that MTC gel did not influence mice growth. Moreover, blood routine examination, blood biochemistry and H&E staining were performed

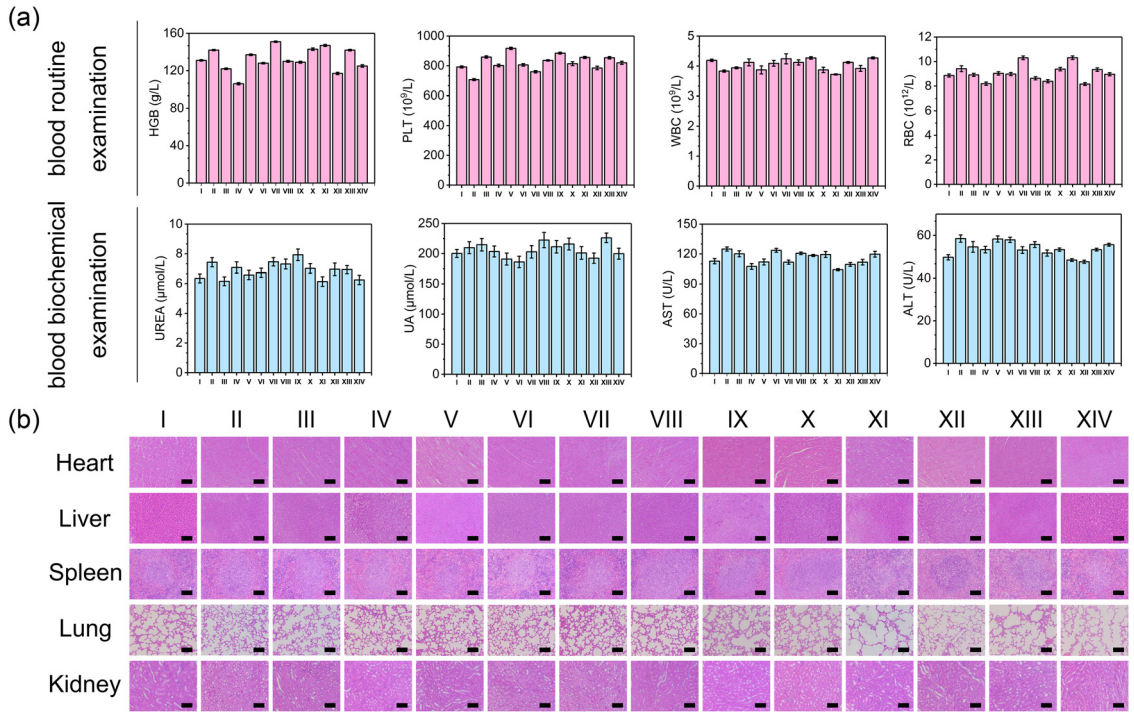

Fig. 7 Biosafety of MTC gel after 14 days of treatment. (a) Levels of blood routine examination indexes (hemoglobin (HGB), platelet (PLT), white blood cells (WBC) and red blood cells (RBC)) and blood biochemical indexes (urea nitrogen (UREA), uric acid (UA), aspartate transaminase (AST) and alanine transaminase (ALT)) respectively (n = 3). (b) Representative H&E staining images of the major organs (heart, liver, spleen, lung, and kidney) of mice harvested from (I) PBS, (II) Blank gel, (III) MnO_2 gel, (IV) MT gel, (V) CaO_2 gel, (VI) MC gel, (VII) MTC gel, (VIII) PBS + Light, (IX) Blank gel + Light, (X) MnO_2 gel + Light, (XI) MT gel + Light, (XII) CaO_2 gel + Light, (XIII) MC gel + Light and (XIV) MTC gel + Light after 14 days of treatment. Scale bar: 100 μm.

to assess the biosafety of MTC gel. As shown in Fig. 7, no apparent difference was detected between the MTC gel + Light treated group and other control groups, demonstrating that MTC gel exhibited negligible toxicity both *in vitro* and *in vivo*.

Conclusions

In summary, an oxygen self-supplying nanozyme-based injectable hydrogel was constructed for reinforced PDT against biofilm infection. The results indicated that the MTC gel possess good mechanical properties and benign injectability. Moreover, benefitting from the good H_2O_2 generation ability of CaO_2 NPs and benign catalase mimic properties of MnO_2 NSs, MTC gel shows enhanced ROS production upon illumination. Both *in vitro* and *in vivo* results indicate that the MTC gel has excellent antibiofilm ability with no side effects on normal tissues. Overall, our designed injectable hydrogel may afford tremendous potential for treating bacterial infections.

Author contributions

Junqing Zhang: conceptualization, methodology, investigation, validation, and writing-original draft. Shuang Zhao: validation, funding acquisition. Shen Zhang: investigation. Hao Zhu: investigation. Yaoxin Zhang: methodology. Linpei Li: methodology. Chaoqun Liu: conceptualization, supervision, writing review, editing, and funding acquisition. Jiahua Shi: conceptualization, supervision, editing, and funding acquisition.

Conflicts of interest

The authors declare no conflicts of interest.

Acknowledgements

This work was financially supported by the National Natural Science Foundation of China (grant no. 22307033, C. L.), the Medical Science and Technology Research Project of Henan Province (grant no. SBGJ202302090, C. L.), the China Postdoctoral Science Foundation (Grant no. 2021M701082, S. Z.), the Key Technologies R&D Program of Henan Province (grant no. 212102310231, C. L.; 222102310209, S. Z.) and the Open Project Program of Key Laboratory for Analytical Science of Food Safety and Biology, Ministry of Education (grant no. FS2204, C. L.).

Notes and references

1 C. Liu, S. Feng, L. Ma, M. Sun, Z. Wei, J. Wang, Z. Chen, Y. Guo, J. Shi and Q. Wu, *ACS Appl. Mater. Interfaces*, 2021, **13**, 38029–38039.
2 S. Zhang, K. Guan, Y. Zhang, J. Zhang, H. Fu, T. Wu, D. Ouyang, C. Liu, Q. Wu and Z. Chen, *Nano Res.*, 2023, **16**, 5346–5356.

3 L. D. Blackman, Y. Qu, P. Cass and K. E. S. Locock, *Chem. Soc. Rev.*, 2021, **50**, 1587–1616.
4 A. S. C. Gonçalves, M. M. Leitão, M. Simões and A. Borges, *Nat. Prod. Rep.*, 2023, **40**, 595–627.
5 H. Zhu, X. Cheng, J. Zhang, Q. Wu, C. Liu and J. Shi, *J. Mater. Chem. B*, 2023, **11**, 618–630.
6 T. M. Uddin, A. J. Chakraborty, A. Khusro, B. M. R. M. Zidan, S. Mitra, T. B. Emran, K. Dhama, M. K. H. Ripon, M. Gajdács, M. U. K. Sahibzada, M. J. Hossain and N. Koirala, *J. Infect. Public Heal.*, 2021, **14**, 1750–1766.
7 M. I. Hutchings, A. W. Truman and B. Wilkinson, *Curr. Opin. Microbiol.*, 2019, **51**, 72–80.
8 O. Ciofu, C. Moser, P. Ø. Jensen and N. Høiby, *Nat. Rev. Microbiol.*, 2022, **20**, 621–635.
9 T. F. Mah, *Future Microbial.*, 2012, **7**, 1061–1072.
10 A. Penesyan, I. T. Paulsen, S. Kjelleberg and M. R. Gillings, *npj Biofilms Microbi.*, 2021, **7**, 80.
11 A. Banerjee, P. Chowdhury, K. Bauri, B. Saha and P. De, *Biomater. Sci-UK.*, 2023, **11**, 11–36.
12 A. K. Abdalla, M. M. Ayyash, A. N. Olaimat, T. M. Osaili, A. A. Al-Nabulsi, N. P. Shah and R. Holley, *Front. Microbiol.*, 2021, **12**, 664395.
13 H. Huang, A. Ali, Y. Liu, H. Xie, S. Ullah, S. Roy, Z. Song, B. Guo and J. Xu, *Adv. Drug Deliver. Rev.*, 2023, **192**, 114634.
14 A. K. Tripathi, P. Thakur, P. Saxena, S. Rauniyar, V. Gopalakrishnan, R. N. Singh, V. Gadhamshetty, E. Z. Gnimpieba, B. K. Jasthi and R. K. Sani, *Front. Microbio.*, 2021, **12**, 754140.
15 S. Qayyum and A. U. Khan, *MedChemComm*, 2016, **7**, 1479–1498.
16 M. Li, Y. Shao, J. H. Kim, Z. Pu, X. Zhao, H. Huang, T. Xiong, Y. Kang, G. Li, K. Shao, J. Fan, J. W. Foley, J. S. Kim and X. Peng, *J. Am. Chem. Soc.*, 2020, **142**, 5380–5388.
17 X. Sun, J. Sun, Y. Sun, C. Li, J. Fang, T. Zhang, Y. Wan, L. Xu, Y. Zhou, L. Wang and B. Dong, *Adv. Funct. Mater.*, 2021, **31**, 2101040.
18 F. F. Sperandio, Y. Y. Huang and M. R. Hamblin, *Recent Pat. Antiinfect. Drug Discov.*, 2013, **8**, 108–120.
19 P. P. Kalelkar, M. Riddick and A. J. García, *Nat. Rev. Mater.*, 2022, **7**, 39–54.
20 K. Villa, H. Sopha, J. Zelenka, M. Motola, L. Dekanovsky, D. C. Beketova, J. M. Macak, T. Ruml and M. Pumera, *Small*, 2022, **18**, 2106612.
21 M. Wu, C. Chen, Z. Liu, J. Tian and W. Zhang, *Acta Biomater.*, 2022, **142**, 242–252.
22 Z. Wang, Y. Zhang, E. Ju, Z. Liu, F. Cao, Z. Chen, J. Ren and X. Qu, *Nat. Commun.*, 2018, **9**, 3334.
23 Y. Dai, Y. Ding and L. Li, *Chin. Chem. Lett.*, 2021, **32**, 2715–2728.
24 A. Wang, G. Fan, H. Qi, H. Li, C. Pang, Z. Zhu, S. Ji, H. Liang, B.-P. Jiang and X.-C. Shen, *Biomaterials*, 2022, **289**, 121798.
25 X. Liu, Z. Yan, Y. Zhang, Z. Liu, Y. Sun, J. Ren and X. Qu, *ACS Nano*, 2019, **13**, 5222–5230.
26 H. Cui, M. Liu, W. Yu, Y. Cao, H. Zhou, J. Yin, H. Liu, S. Que, J. Wang, C. Huang, C. Gong and G. Zhao, *ACS Appl. Mater. Interfaces*, 2021, **13**, 26800–26807.
27 D. Jiang, D. Ni, Z. T. Rosenkrans, P. Huang, X. Yan and W. Cai, *Chem. Soc. Rev.*, 2019, **48**, 3683–3704.
28 H. Wang, W. Yang, X. Wang, L. Huang, Y. Zhang and S. Yao, *Sens. Actuators, B*, 2020, **304**, 127389.
29 J. Saroia, W. Yanen, Q. Wei, K. Zhang, T. Lu and B. Zhang, *Bio-Des. Manuf.*, 2018, **1**, 265–279.
30 E. M. Ahmed, *J. Adv. Res.*, 2015, **6**, 105–121.
31 S. Wang, H. Zheng, L. Zhou, F. Cheng, Z. Liu, H. Zhang and Q. Zhang, *Biomaterials*, 2020, **260**, 120314.
32 L. Yang, S.-T. D. Chueng, Y. Li, M. Patel, C. Rathnam, G. Dey, L. Wang, L. Cai and K.-B. Lee, *Nat. Commun.*, 2018, **9**, 3147.
33 J. Zheng, W. Wang, X. Gao, S. Zhao, W. Chen, J. Li and Y.-N. Liu, *Small*, 2022, **18**, 2205252.
34 S. Dong, Y. Chen, L. Yu, K. Lin and X. Wang, *Adv. Funct. Mater.*, 2020, **30**, 1907071.
35 J. Zhao, J. Li, C. Zhu, F. Hu, H. Wu, X. Man, Z. Li, C. Ye, D. Zou and S. Wang, *ACS Appl. Mater. Interfaces*, 2018, **10**, 3392–3404.
36 K. Kai, Y. Yoshida, H. Kageyama, G. Saito, T. Ishigaki, Y. Furukawa and J. Kawamata, *J. Am. Chem. Soc.*, 2008, **130**, 15938–15943.
37 Y. Liu, S. Chi, Y. Cao and Z. Liu, *ACS Appl. Nano Mater.*, 2022, **5**, 2592–2602.
38 C. Tu, H. Lu, T. Zhou, W. Zhang, L. Deng, W. Cao, Z. Yang, Z. Wang, X. Wu, J. Ding, F. Xu and C. Gao, *Biomaterials*, 2022, **286**, 121597.
39 A. Y. Sychev and V. Isak, *Russ. Chem. Rev.*, 1993, **62**, 279.

